Petroleum Science 20 (2023) 1947–1960

Contents lists available at ScienceDirect

Petroleum Science

journal homepage: www.keaipublishing.com/en/journals/petroleum-science

Original Paper

Quantitative characterization of shale pore connectivity and controlling factors using spontaneous imbibition combined with nuclear magnetic resonance T_2 and T_1-T_2

Peng-Fei Zhang [a], Shuang-Fang Lu [b, *], Jun-Qian Li [c], Xiang-Chun Chang [a], Jun-Jian Zhang [a], Yu-Mao Pang [a], Zi-Zhi Lin [c], Guo Chen [d], Ya-Jie Yin [a], Yu-Qi Liu [a]

[a] College of Earth Science and Engineering, Shandong University of Science and Technology, Qingdao, 266590, Shandong, China
[b] Sanya Offshore Oil & Gas Research Institute, Northeast Petroleum University, Sanya, Hainan, 572025, China
[c] Key Laboratory of Deep Oil and Gas, China University of Petroleum (East China), Qingdao, 266580, Shandong, China
[d] College of Resources and Environment, Yangtze University, Wuhan, 430100, Hubei, China

ARTICLE INFO

Article history:
Received 16 July 2022
Received in revised form
20 September 2022
Accepted 15 March 2023
Available online 17 March 2023

Edited by Jie Hao and Teng Zhu

Keywords:
Pore connectivity
Spontaneous imbibition
Nuclear magnetic resonance
Mercury intrusion capillary pressure
Shale oil reservoir

ABSTRACT

Shale oil can be extracted from shale by using interconnected pore networks. The migration of hydrocarbon molecules within the shale is controlled by pore connectivity. However, assessing the pore connectivity of shale oil reservoirs is uncommon. To characterize pore connectivity and clarify its controlling factors, this study used spontaneous imbibition (SI) combined with nuclear magnetic resonance (NMR) T_2 and T_1-T_2 technologies on shale oil reservoirs selected from the Shahejie Formation in the Dongying Sag, Bohai Bay Basin. According to the findings, the SI processes of shales include fast-rising, slow-rising, and stable stages. The fast-rising stage denotes pore connectivity. The shales studied have poor connectivity, with lower imbibition slopes and connected porosity ratios, but large effective tortuosity. During the SI process, micropores have the highest imbibition saturation, followed by mesopores and macropores. Furthermore, n-dodecane ingested into micropores appears primarily as adsorbed, whereas n-dodecane appears primarily as free states in mesopores and macropores during the SI process. The pore connectivity of the shales under study is primarily controlled by inorganic minerals. Quartz and feldspar develop large and regular pores, resulting in better pore connectivity, whereas clay minerals and calcite with plenty of complex intragranular pores do not. Organic matter negatively influences pore connectivity because the dissolution of calcite by organic acid produced during hydrocarbon generation leads to a more complex and heterogeneous pore structure. This study sheds light on the pore connectivity and controlling factors of the shale oil reservoir and aids in the understanding of shale oil mobility.

1. Introduction

Shale oil is mature oil found in organic-rich shales and tight sandstone or carbonate rock interlayers (i.e., the shale series) (Zou et al., 2020). Shale oil has received increasing attention because of its vast source. Shale oil has recently been extracted from several Chinese continental basins, including the Permian Lucaogou Formation in the Jimusaer Depression, the Paleogene Shahejie Formation in the Bohai Bay Basin, and the Cretaceous Qingshankou Formation in the Songliao Basin (Liu et al., 2017a,b; Zou et al., 2018; Xu et al., 2019; Liu et al., 2021; Jin et al., 2022). However, compared to the vast resource, shale oil production is significantly lower. The critical factor influencing successful shale oil development is mobility, which is primarily controlled by shale oil composition and occurrence state, as well as reservoir characteristics (Lu et al., 2016).

The higher the saturated, light hydrocarbons and gas-oil ratio in shale oil, the better the mobility and ease of production, corresponding to the higher recoverability of medium-high maturity shale oil (Jin et al., 2021). Shale oil is found in both adsorbed and free states. Adsorbed oil is nearly immobile, including oil that is mutually soluble (absorbed) in organic matter (kerogen) and

* Corresponding author.
E-mail address: lushuangfang@nepu.edu.cn (S.-F. Lu).

https://doi.org/10.1016/j.petsci.2023.03.011

adsorbed on the surface of inorganic mineral particles (Li et al., 2017a;2018a,b). Free oil is primarily found in larger pores and fractures that are potentially producible and movable (Zhang et al., 2022). Shale oil mobility is also influenced by reservoir characteristics. However, previous research has primarily focused on porosity, permeability, pore type, pore size distribution, and so on (Tian et al., 2021; Zeng et al., 2021, 2022; Li et al., 2022; Liu et al., 2022a), whereas pore connectivity is the critical factor limiting shale oil mobility. However, assessing pore connectivity within shale oil reservoirs is uncommon. Pore connectivity is the degree of connectivity of the pore (throat) system, which is generally defined by connected porosity, pore ratio, matrix permeability, tortuosity, pore-throat ratio, and so on. Pore connectivity limits both shale oil enrichment and percolation. Typically, the greater the pore connectivity, the greater the oil saturation and mobility, implying higher productivity and a "sweet point".

Because of the mixed wetting, complex mineral composition, heterogeneous pore structure, and other factors, assessing pore connectivity in shale is difficult. To investigate shale pore connectivity, digital cores derived from three-dimensional imaging technology, such as X-ray computed tomography and focused ion beam-scanning electron microscopy (FIB-SEM), were used (Kelly et al., 2016; Wang et al., 2016). The findings revealed that pore connectivity in shale is poor. The high resolution, however, implies a small field of view, implying that the digital core may not be representative. Furthermore, because most throats in shale are less than the resolution, imaging technology cannot detect most of the throats connecting pores. As a result, imaging technology's assessment of pore connectivity is generally poor. Pore network modeling can also be used to create a digital core, though it may not correspond to the actual shale (Wang and Shen, 2018). Mercury intrusion capillary pressure (MICP) is regarded as an effective technology for detecting connected pores, as it provides a variety of parameters to characterize pore connectivity, such as connected porosity, matrix permeability, tortuosity, and so on (Huang and Zhao, 2017). Better connectivity is indicated by higher connected porosity and lower tortuosity.

Spontaneous imbibition (SI) is a process in which the wetting phase fluid is spontaneously imbibed into the pores to displace the non-wetting phase by the capillary pressure (Gao et al., 2019). In the initial stage of the SI process, the capillary pressure is the largest, and the wetting phase fluid is rapidly imbibed into the pore network. Then, with the wetting phase fluid intake increasing, the capillary force gradually decreases. Thus, SI is an alternative experiment for assessing pore connectivity (Gao and Hu, 2016; Gao et al., 2018; Wang et al., 2018; Wu et al., 2018; Xue et al., 2022). The imbibition slope (k) of the SI experiment between the height of cumulative imbibition and imbibition time can accurately reflect the pore connectivity. According to the SI percolation theory, a higher k value generally implies better pore connectivity (Handy, 1960). Furthermore, nuclear magnetic resonance (NMR) is a non-destructive and efficient technology, and T_2 technology can monitor the SI experiment to elucidate the inhalation process of fluid (oil or water) in shale pores at different scales (Zhang et al., 2018a; Zheng et al., 2019; Zhao et al., 2019). SI-NMR is a powerful method to analyze pore connectivity and simultaneously monitor the dynamic process of shale pore fluids. Recently, SI-NMR experiments were conducted to reveal pore connectivity and its influencing factors (Meng et al., 2015a, 2015b; Huang and Zhao, 2017; Ren et al., 2018; Wang et al., 2021). Meng et al. (2015a) demonstrated that the counter-current SI of shale reduces the damage caused by the aqueous phase trapping more than the co-current SI. The SI-NMR experiments on low-medium maturity shales revealed that pore connectivity varies at different scales (Wang et al., 2021). Micropores (<100 nm) have the best connectivity, followed by mesopores (100–1000 nm) and macropores (>1000 nm). However, few studies have paid attention to the dynamic changes of fluid occurrence states in pores with different scales during the SI process. T_1-T_2 technology can well characterize the occurrence states during the SI process. Thus, SI combined with NMR T_2 and T_1-T_2 technologies can accurately reveal the pore connectivity and fluid occurrence states within shales.

Furthermore, pore connectivity is influenced by a variety of factors, such as pore type, organic matter, mineral composition, etc. Intergranular pores in inorganic minerals typically have the best connectivity, whereas intragranular pores (including dissolution pores) are generally poorly connected (Yang et al., 2019). Because organic pores are lipophilic and have better connectivity, they control the pore connectivity of shale gas reservoirs (Gao and Hu, 2016). The Jurassic Ziliujing Formation shales SI experiments revealed that the quartz content primarily controls pore connectivity, and higher porosity indicates better water-wet pore connectivity (Gao et al., 2018). According to Wang et al. (2021), the pore connectivity of low-medium maturity shale is primarily related to the production index, organic matter maturity, and calcite, but not TOC or other minerals. As a result, the factors influencing pore connectivity may differ from marine to continental or from low to high (over) maturity shales.

This study aims to evaluate pore connectivity and identify the factors that influence it in shale oil reservoirs. Thus, shale from the Shahejie Formation in the Dongying Sag, Bohai Bay Basin, was sampled to characterize the imbibition process using SI-NMR. Furthermore, SI-NMR experiments were performed on dry and cleaned samples to evaluate the pore connectivity of the shale matrix. Meanwhile, measurements of TOC, rock pyrolysis, MICP, and X-ray diffraction (XRD) were done to investigate the influencing factors.

2. Methodology

2.1. Samples and experiments

Shales were sampled from the Paleogene Shahejie Formation, Dongying Sag, Baihai Bay Basin. A total of 13 samples were collected. The geological setting of the area under study and the sampling wells are shown in Fig. 1, which has been described in detail in the authors' previous publications (Zhang et al., 2018b, 2022). Shale samples were cut into 25 mm diameter core plugs parallel to the bedding direction. The core plugs were further subdivided into four parts: two end cuttings and two plugs. The TOC, Rock-Eval, and XRD tests were carried out on the two end cuttings. SI and NMR experiments were performed on one core plug, while MICP measurements were performed on another.

2.1.1. MICP

Prior to the tests, all of the shale core plugs were cleaned in a modified soxhlet extractor for 72 h in dichloromethane and acetone-mixed solution (3:1) to remove any residual oil at 90 °C and 0.3 MPa. The cores were then dried in a vacuum oven at 110 °C (pressure less than −0.1 MPa) to remove the residual oil and water in shale pores. The MICP tests were performed on the Micromeritics AutoPore 9520 Porosimeter, with an injection pressure of up to 200 MPa, corresponding to a pore-throat size of approximately 7 nm.

2.1.2. SI-NMR

The core plugs had a length of 10–20 mm and a diameter of 25 mm. To examine the pore connectivity of the shale matrix, the core plugs were cleaned using the same method to remove all residual fluid within shales before the SI experiments. The T_2 and T_1-

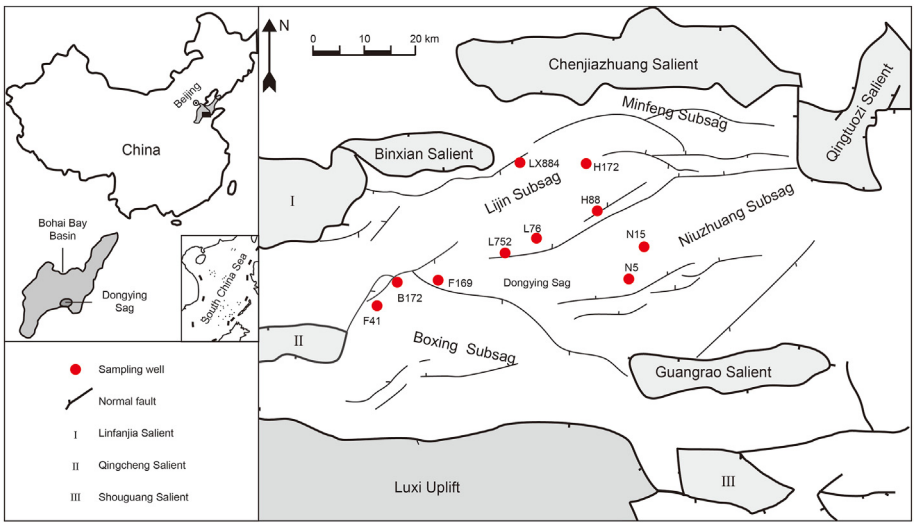

Fig. 1. Sampling location and geological setting of the study area (after Zhang et al., 2022).

Table 1
Organic matter and mineral compositions of shale samples.

Sample	Organic matter			Mineral composition, %					
	TOC, %	S_1, mg/g	T_{max}, °C	Clay	Quartz	Feldspar	Orthoclase	Calcite	Dolomite
B172-1	2.06	1.5014	443	30.3	12.2	1.9	0.0	42.6	7.5
B172-3	0.87	0.1776	440	14.8	35.5	10.3	2.5	6.1	30.8
F169-3	0.59	0.1163	444	45.5	24.8	7.3	1.3	11.8	9.3
F169-4	1.28	4.0867	428	7.8	46.8	31.5	2.9	8.3	2.7
F41-2	1.66	0.2880	439	14.0	38.7	18.5	5.8	11.2	6.6
F41-3	1.19	1.4087	434	13.2	33.3	32.2	8.5	8.3	4.5
H172-1	3.15	2.0967	441	43.9	19.6	1.1	0.5	26.9	1.0
H88-2	1.70	0.2335	443	46.2	21.3	5.5	4.7	12.0	5.9
L752-2	0.60	0.1161	449	46.1	26.3	11.1	4.3	3.5	4.8
L76-2	0.36	0.0942	452	28.9	40.0	14.2	2.8	1.8	8.9
LX884-1	2.52	2.9565	443	30.0	26.0	2.7	0.2	18.7	17.5
N15-1	2.25	1.2164	441	25.5	13.1	6.8	1.3	41.3	8.9
N5-3	0.16	0.1232	487	2.6	43.0	16.8	5.1	14.7	14.0

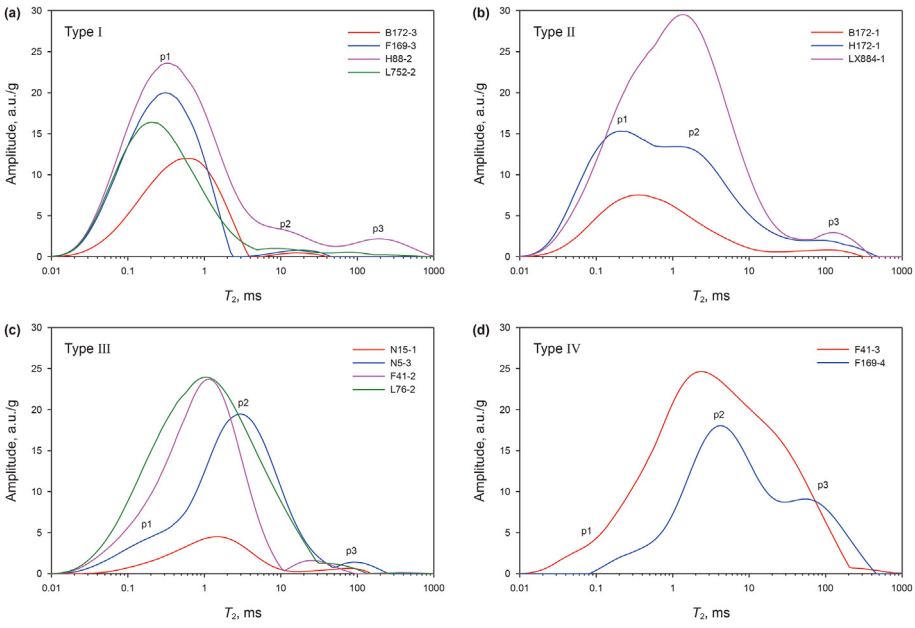

Fig. 2. NMR T_2 spectral of n-dodecane saturated shales without dry sample signals.

Table 2
Pore structure parameters of shales obtained from MICP and NMR tests.

Sample	MICP					NMR		φ_M/φ_N
	φ_M	d_{ac}	τ	L_e/L	K_c	φ_N	$T_{2,gm}$	
B172-1	0.85	13.49	534.79	23.2	1	3.05	0.67	0.28
B172-3	2.27	18.35	100.08	17.54	56	3.98	0.45	0.57
F169-3	2.86	11.49	198.94	25.68	6	6.31	0.29	0.45
F169-4	7.15	112.73	5.53	6.79	46994	7.85	9.01	0.91
F41-2	7.17	26.75	44.03	18.68	318	7.38	1.15	0.97
F41-3	10.78	88.76	4.64	7.5	73439	12.37	4.37	0.87
H172-1	2.25	14.46	265.24	29.89	11	7.81	0.88	0.29
H88-2	4.42	14.6	92.89	21.03	22	8.92	0.62	0.50
L752-2	2.27	12.76	314.48	29.08	5	5.56	0.31	0.41
L76-2	6.69	29.84	24.44	13.68	560	9.89	1.03	0.68
LX884-1	6.62	12.03	157.18	34.11	17	12.49	1.15	0.53
N15-1	1.45	13.53	211.48	18.08	2	1.46	1.41	0.99
N5-3	4.56	52.24	16.46	8.86	2434	6.64	2.21	0.69

φ_M is the porosity obtained from MICP test, %; d_{ac} refers to the average pore diameter from MICP, nm; τ and L_e/L are the effective and geometrical tortuosity, respectively; K_c is the matrix permeability from MICP, 10^{-9}μm^2; φ_N denotes the NMR porosity, %; $T_{2,gm}$ represents the geometric mean of T_2 spectrum at saturation condition, ms.

T_2 spectra of dry shales were detected after cooling to room temperature in a desiccator. The medium for the SI experiment was n-dodecane fluid, which was evacuated for 24 h to remove dissolved air. The SI experiments in this study were carried out in a counter-current flow condition. After removing the surface fluid, the shale masses were tested at specific intervals with an electronic balance (0.0001 g). Meanwhile, the T_2 and T_1-T_2 spectra were measured. The number of T_2 spectra obtained during the SI experiment for each shale sample ranges from 7 to 13. And a total of 3 T_1-T_2 spectra were collected for each sample to analyze the changes in occurrence states of fluid during the SI process.

Following the SI-NMR experiments, all the samples were cleaned and dried in the same manner. Following that, the shales were saturated with n-dodecane, and the T_2 and T_1-T_2 spectra at saturation were measured. And, as discussed in the authors' study, the NMR porosity was calculated using the T_2 spectra of dry shales as background signals (Zhang et al., 2019).

NMR measurements were taken using a MesoMR23-60H-I NMR spectrometer in this study. The CPMG and IR-CPMG sequences were used to test the T_2 and T_1-T_2 spectra. TW = 3000 ms, TE = 0.07 ms, NECH = 6000, and NS = 64 were the CPMG sequence parameters (Zhang et al., 2019). The IR-CPMG sequence parameters were set to correspond to CPMG, with the addition of NS = 32 and NTI = 25 (Zhang et al., 2022).

2.2. Pore structure parameters calculated by MICP

MICP can provide various pore structure parameters. The permeability can be calculated using the Katz and Thompson (K-T) method (Katz and Thompson, 1986, 1987) based on the mercury intrusion curves:

$$K = \frac{1}{89}\frac{L_{\max}}{L_c}\varphi S_{L_{\max}} \tag{1}$$

where K refers to the matrix permeability, μm^2; φ is the porosity obtained from MICP, %; $L_{\max}$ denotes the pore throat diameter when the hydraulic is maximum, μm; L_c represents the threshold pore throat diameter, μm; $S_{L\max}$ refers to the mercury saturation at $L_{\max}$, %.

Then, the effective tortuosity (τ) can be calculated as follows (Hager, 1998; Webb, 2001):

$$\tau = \sqrt{\frac{\rho}{24K(1+\rho V_t)}\int_{r_{c,\min}}^{r_{c,\max}} r_c^2 f_v(r_c)\mathrm{d}r_c} \tag{2}$$

where ρ denotes the density of mercury, cm^3/g; V denotes the pore volume, cm^3/g; $\int_{r_{c,\min}}^{r_{c,\max}} r_c^2 f_v(r_c)\mathrm{d}r_c$ represents the probability density function of pore throat. Meanwhile, the geometrical tortuosity (L_e/L) can also be obtained by Eq. (3) (Epstein, 1989).

$$\tau = \frac{1}{\varphi}\left(\frac{L_e}{L}\right)^2 \tag{3}$$

3. Results

3.1. Shale sample characteristics

3.1.1. Organic matter and mineral compositions

The TOC contents of the selected shales range from 0.16% to 3.15%, with an average of 1.41%, and the S_1 contents are between 0.0942 mg/g and 4.0567 mg/g (mean 1.1089 mg/g), as shown in Table 1. The organic matter ranges from low to maturity, as indicated by a T_{max} of 428–487 °C. Clay minerals, quartz, calcite, and feldspar make up most of the shale samples, with average values of 26.8%, 29.3%, 15.9%, and 12.3%, respectively. The selected samples include various types of shale oil reservoirs based on organic matter and mineral compositions.

3.1.2. Pore structures

Fig. 2 shows the NMR T_2 spectra of n-dodecane saturated shale samples from which the dry sample signals were subtracted as discussed in the authors' previous study to characterize the pore structure (Zhang et al., 2019). The T_2 spectra of shales show three peaks. The first peak (p1) is primarily located at T_2 less than 1 ms, while the second peak (p2) is located between 1 ms and 20 ms.

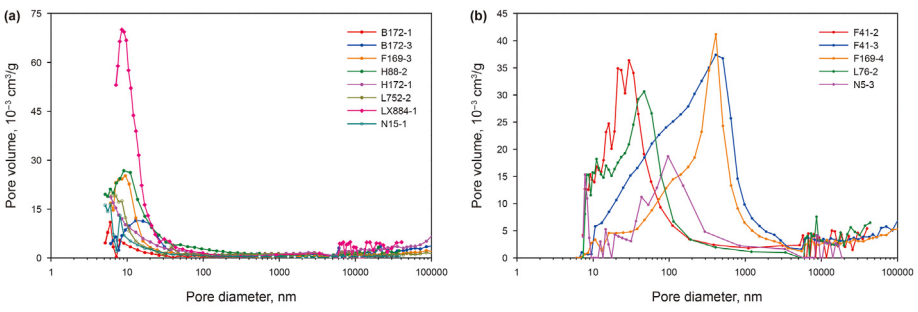

Fig. 3. Pore-throat size distributions of shales obtained from MICP.

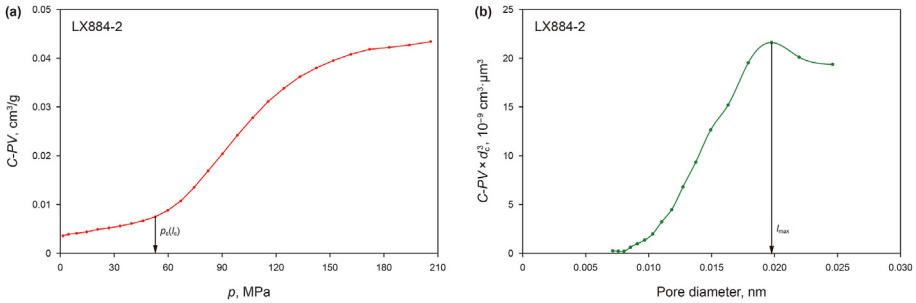

Fig. 4. Determinations of L_c and L_{max} for calculating shale matrix permeability using MICP.

Furthermore, the third peak (p3) lasted longer than 20 ms. The p1, p2, and p3 represent micropores, mesopores, and macropores, respectively (Zhang et al., 2018a, b). The NMR porosity can be calculated by subtracting the amplitude of the saturated shale signals from the dry sample signals. The NMR porosity (φ_N) ranges from 1.46% to 12.49%, with an average of 7.21%, referring to shales' total porosity (Table 2).

MICP is a powerful technology for detecting connected pores in shales and characterizing accessible (connected) porosity, permeability, effective tortuosity (τ), and other parameters. Generally, the better the pore connectivity of shale, the higher the connected porosity and its proportion, the greater the permeability, and the lower the effective tortuosity of shale. The connected porosity (φ_M) of 13 samples ranges from 0.85% to 10.78%, with a mean of 4.56%. The ratio of MICP to NMR porosity (φ_M/φ_N) denote shale pore connectivity in the range of 0.28–0.99 (mean 0.63), indicating poor pore connectivity in shales. According to the MICP measurements, the pore throats within the shale matrix are mostly less than 5 μm (Fig. 3). Pore-throats are typically less than 50 nm in most shale samples, as shown in Fig. 3a. Furthermore, the average pore-throat diameters (d_{ac}) obtained from MICP ranged from 11.49 to 112.73 nm (mean 32.39 nm).

When calculating permeability from MICP, Eq. (1) states that the L_c and L_{max} should be determined first. L_c is the pore-throat diameter associated with the critical pressure (p_c) on cumulative pore volume (*C-PV*) and mercury injection pressure (p). As shown in Fig. 4a, when p is less than p_c, the *C-PV* increases slowly as p increases. When p is greater than p_c, however, the *C-PV* increases rapidly as p increases (Katz and Thompson, 1986). As shown in Fig. 4b, the L_{max} is the pore diameter corresponding to the maximum value of the cumulative pore volume × pore diameter ^{3} (*C-PV* × d_c^3) ~ pore diameter curve (Katz and Thompson, 1987). According to the results, the permeability (K_c) calculated by MICP ranges from 1–73439 × 10^{-9} μm^2, with most values less than 20 × 10^{-9} μm^2, indicating poor pore connectivity.

The effective tortuosity can be determined using the MICP permeability and Eq. (2), and the geometrical tortuosity (L_e/L) can be calculated using Eq (3). Shale has an effective tortuosity of 4.64–534.79 (mean 151.55) and a geometrical tortuosity of 6.79–34.11 (mean 19.55) (Table 2). The high effective and geometrical tortuosity values in the studied shales indicate poor pore connectivity.

3.2. Pore connectivity characterized by the SI

SI experiments were performed on 13 shale samples in this study, and the SI curves are shown in Fig. 5. Because the lengths of all core plugs for SI experiments in this study are less than 20 mm,

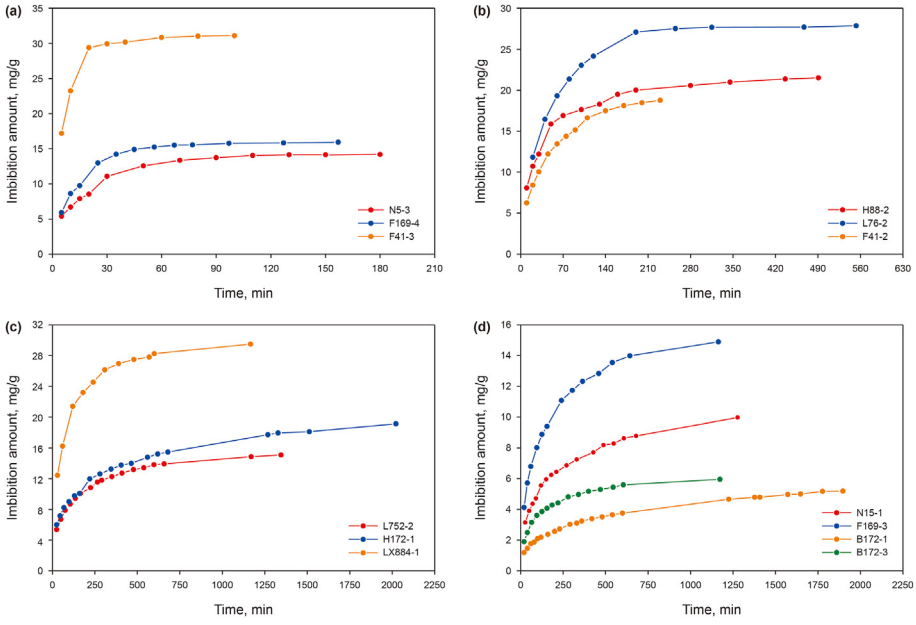

Fig. 5. Spontaneous imbibition oil curves of shales.

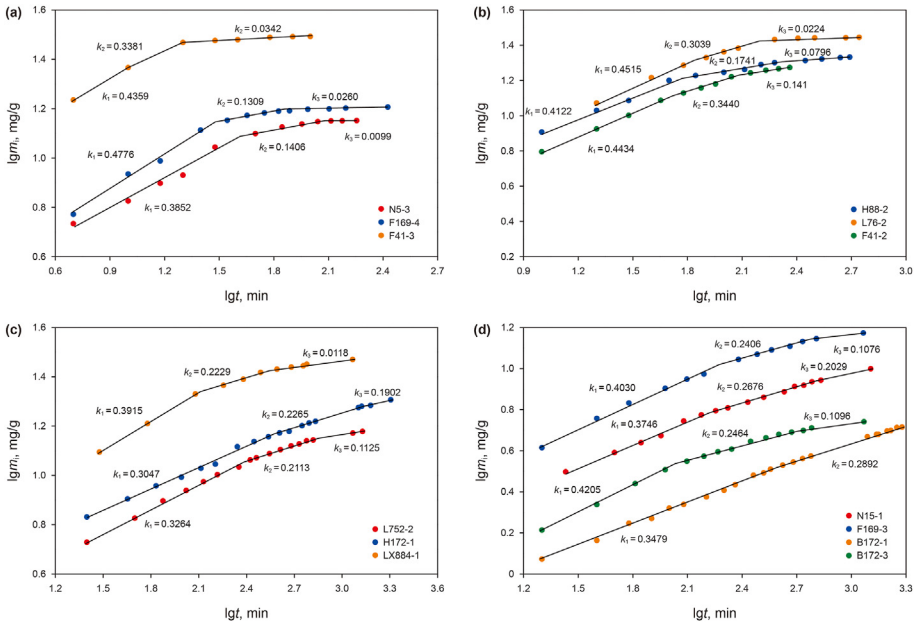

Fig. 6. Spontaneous imbibition slopes of shales.

the effect of gravity forces can be minimized. The capillary pressure is dominant in the initial stages of SI and gradually decreases as SI saturation (time) increases. As a result, the amounts of shale SI increase rapidly over time, followed by a gradual decrease in SI rates. Finally, weaker capillary pressure is unable to drive fluid into pore systems, and SI reaches equilibrium states. However, the time for shale SI to reach the equilibrium state varies depending on the pore structure. The faster the SI rate and the faster the equilibrium state is reached, the better the pore structure. Sample F41-3, for example, achieves equilibrium in less than 120 min, whereas Sample B17-1 requires approximately 2000 min (Figs. 2, 3 and 5).

If gravity forces are ignored, the Handy equation shows that the cumulative imbibition height (or amount) (m) has a linear relationship with the square-root-of-time ($t^{0.5}$) in the porous material (Handy, 1960). Thus, for the homogeneous porous material, a slope (imbibition slope) of 0.5 is obtained between the cumulative imbibition amount and time on log-log coordinates. Furthermore, the imbibition slope is a useful parameter for assessing pore connectivity in porous media. Imbibition slopes of less than 0.5 indicate poor connectivity.

As shown in Fig. 6, the cumulative imbibition amount (m_i) versus time (t) of the shales under this study is plotted in log-log coordinates. Except for Sample B172-1, the log-log plots show three linear segments, including fast-rising, slow-rising, and stable stages. The imbibition slope (k_1) value is greatest in the fast-rising stage, and the SI amount increases rapidly. As a result, the slow-rising stage's imbibition slope (k_2) value decreases, while the stable stage's imbibition slope (k_3) value is the lowest, corresponding to the equilibrium states.

Table 3 shows the imbibition slope values (k_1, k_2, and k_3). k_1 ranges from 0.3027 to 0.4776, with an average of 0.3980. The values of k_2 are between 0.1309 and 0.3440 (mean 0.2422), while the k_3 value is 0.0099–0.2029 (mean 0.0932). Meanwhile, the SI saturations of n-dodecane in these three stages have been calculated and are shown in Table 3. The SI saturation of the fast-rising stage (S_{o1}) ranges from 36.78% to 85.21% (mean 61.94%), and it is positively related to k_1. The slow-rising stage (S_{o2}) SI saturation is 58.84%–95.40% (mean 80.72%), and the final SI saturation (S_{ot}) is 58.94%–98.78% (mean 85.84%). Fig. 7 depicts the relationships between k_1, k_2, and k_3. There is a weak negative correlation between k_1 and k_3,

Table 3
Slope values and saturations of spontaneous imbibition.

Sample	k_1	k_2	k_3	S_{o1},%	S_{o2}, %	S_{ot}, %
B172-1	0.3479	0.2892	/	36.78	58.94	58.94
B172-3	0.4205	0.2734	0.1189	65.00	95.40	95.40
F169-3	0.403	0.2406	0.1076	41.82	60.30	66.34
F169-4	0.4776	0.1309	0.026	61.96	74.01	76.87
F41-2	0.4434	0.344	0.141	62.07	84.54	95.48
F41-3	0.4359	0.3381	0.0342	85.21	90.15	90.15
H172-1	0.3047	0.2118	0.1796	64.60	87.53	93.40
H88-2	0.4122	0.1741	0.0796	62.82	79.23	85.17
L752-2	0.3264	0.2113	0.1125	54.89	70.60	76.49
L76-2	0.4515	0.3039	0.0244	72.22	90.25	90.25
LX884-1	0.3915	0.2229	0.0818	68.21	83.38	94.08
N15-1	0.3746	0.2676	0.2029	58.94	85.35	98.78
N5-3	0.3852	0.1406	0.0099	70.69	89.70	90.61

k_1, k_2, and k_3 are the imbibition slopes of fast-rising, slow-rising, and stable stages, respectively; S_{o1}, S_{o2}, and S_{ot} are the imbibition saturations of fast-rising, slow-rising, and stable stages, respectively.

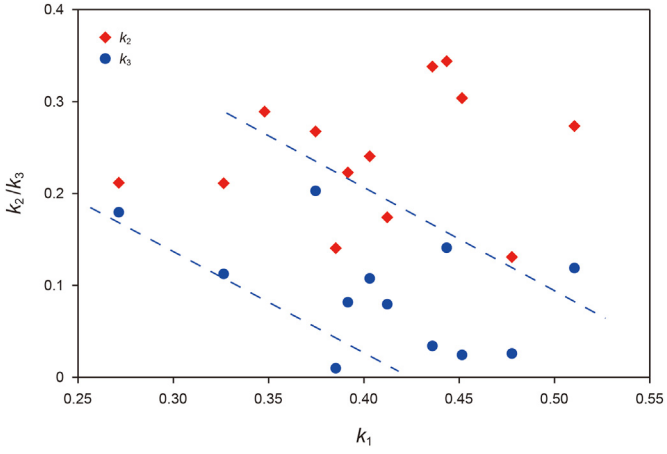

Fig. 7. Relationships among k_1, k_2, and k_3.

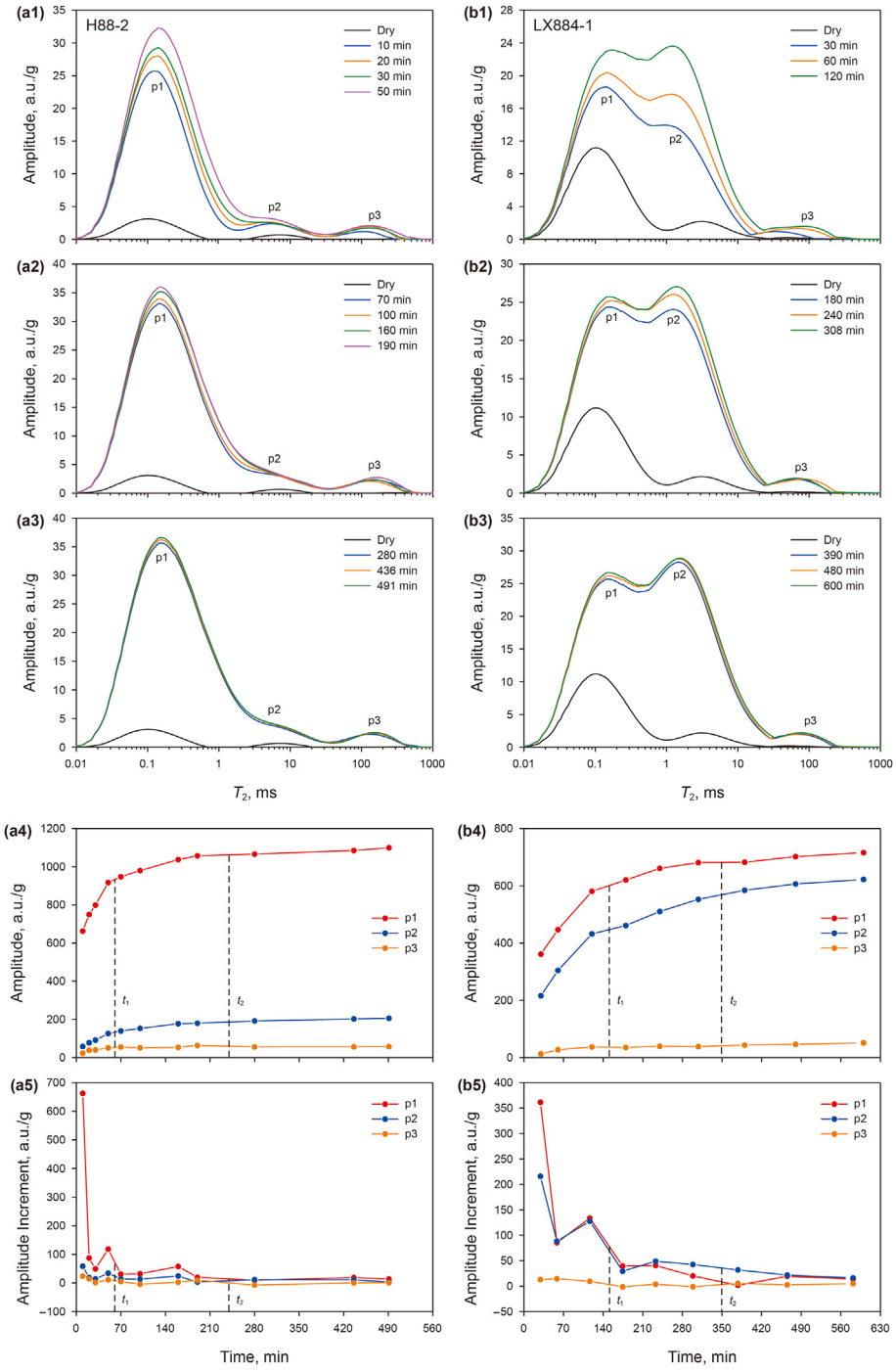

Fig. 8. NMR T_2 spectral during spontaneous imbibition (Samples H88-2 and LX884-1).

but no obvious correlation between k_1 and k_2. As a result, in this study, the imbibition slope of the fast-rising stage (k_1) is regarded as the most effective indicator of pore connectivity in shales. All of the k_1 values, however, are less than 0.5, indicating poor connectivity. As a result, it is possible to conclude that the pore system connectivity of the shales under this study is poor.

3.3. NMR T_2 and T_1-T_2 spectra during the SI

3.3.1. NMR T_2 spectra

The NMR T_2 spectra during the SI process are depicted in Figs. 8 and 9. The shales under study can be classified into four types based on the T_2 spectrum distributions shown in Fig. 2. Type I has the largest p1, but small p2 and p3, indicating lots of micropores and a little bit of meso- and macropores (B172–3, F169–3, H88-2, and L752-2) (Fig. 2a). When the peak amplitude is nearly stable, one type of pore is considered to have completed the imbibition. Using the H88-2 as an example, as shown in Fig. 8a1–a3, p2, and p3 stabilize quickly, while p1 gradually increases with time, as evidenced by the amplitudes of p1, p2, and p3 (Fig. 8a4–a5). The findings imply that n-dodecane imbibition occurs almost simultaneously in all pores, including micropores, mesopores, and macropores. This phenomenon indicates that if the shale contains numerous micropores, the mesopores and macropores are

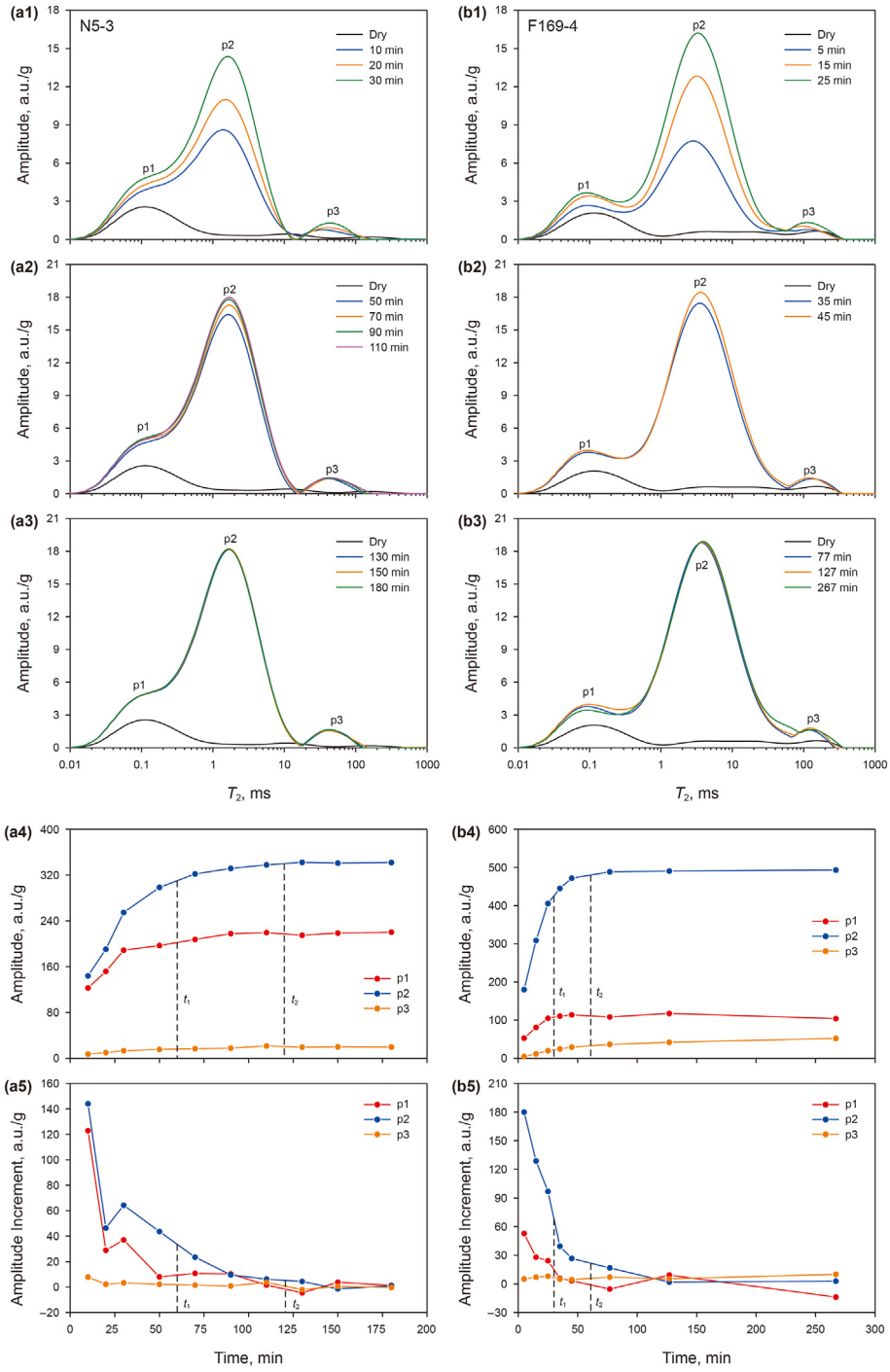

Fig. 9. NMR T_2 spectral during spontaneous imbibition (Samples N5-3 and F169-4).

primarily regarded as seepage channels, and the n-dodecane preferentially enters during the SI, resulting in rapid stabilization of the p2 and p3. Furthermore, n-dodecane imbibition in Type I shale is primarily controlled by micropores, with lower imbibition slopes averaging 0.3905 (Table 3 and Fig. 5), indicating poor connectivity pore systems in Type I shales.

The significant characteristics of Type II shales, including three samples (B172–1, H172-1, and LX884-1) are large p1 and p2, but small p3 (Fig. 2b). Consider the LX884-1, the p3 stabilizes quickly, as shown in Fig. 8b. Furthermore, the imbibition rate of micropores is greater than that of mesopores, implying that the amplitude of p1 increases faster than that of p2 due to the higher capillary pressure of micropores than that of the mesopores. The n-dodecane imbibition of Type II shale is primarily controlled by micropores and mesopores, with the lowest imbibition slope (mean 0.3480) due to the smallest average pore-throat size (mean 13.39 nm) (Tables 2 and 3), implying the poorest connectivity.

Type III shales have the highest p2, the lowest p1, and the minor p3, corresponding to a huge number of mesopores, moderate micropores, and few macropores, with four samples (N15–1, N5-3, F41-2, and L76-2) exhibiting these characteristics (Fig. 2c). Taking the N5-3 as an example (Fig. 9a), which is similar to Type II shale,

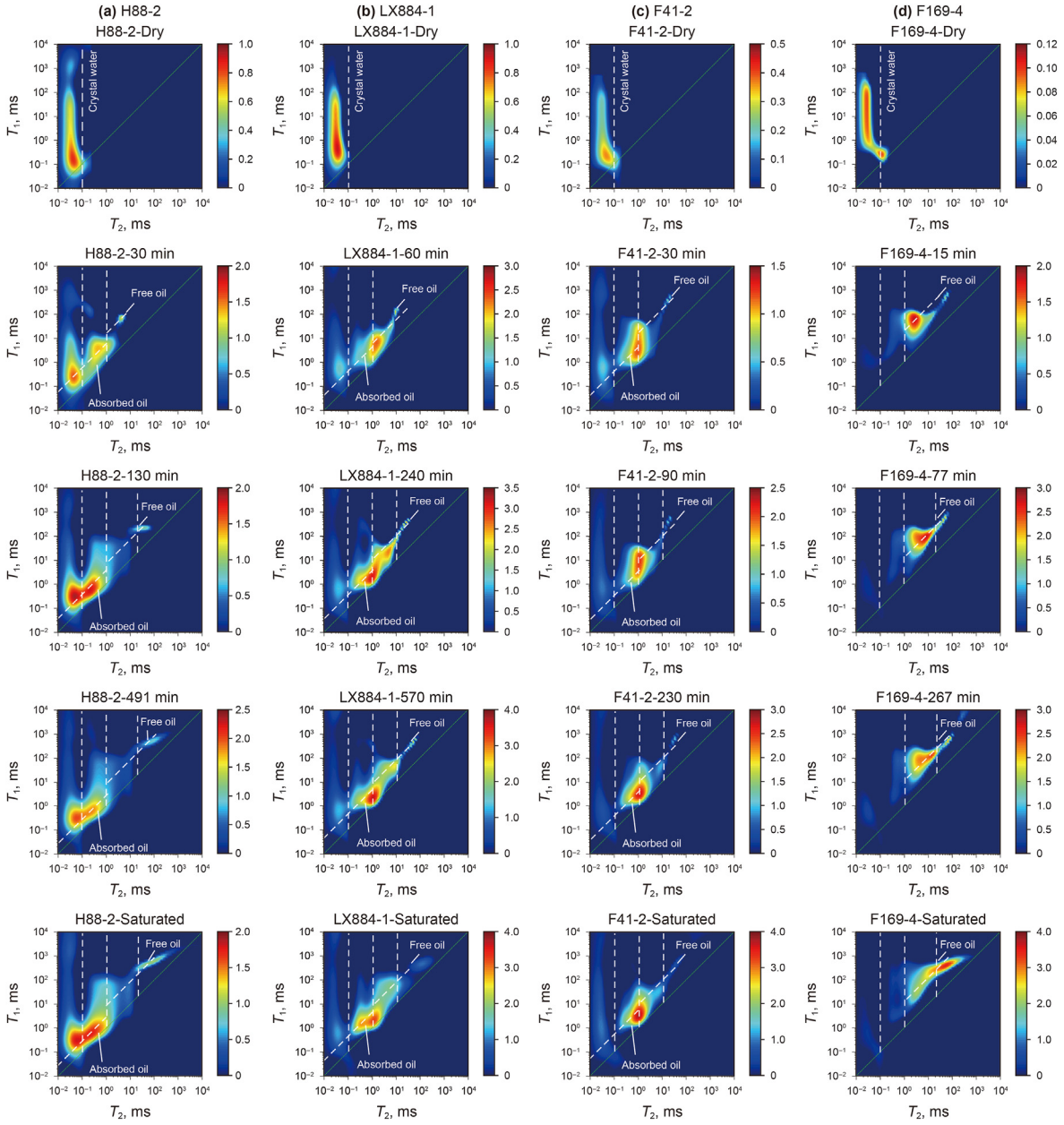

Fig. 10. NMR T_1-T_2 spectral during spontaneous imbibition.

the macropores are the dominant seepage channel and the p3 stabilizes quickly. Meanwhile, p1 stabilized faster than p2. The mesopores, on the other hand, regulate n-dodecane imbibition. Type III shales have an average imbibition slope of 0.4137, indicating better connectivity (Table 3). Type IV shale has large p2 and p3 but small p1, indicating that there are many mesopores and macropores but only a few micropores (Fig. 2d). The macropore with a large pore size has a lower capillary pressure. As a result, macropore imbibition stabilized quickly, and imbibition saturation was reduced (Fig. 9b). Meanwhile, micropore imbibition is faster than mesopore imbibition. Type IV shales have the best connectivity and the steepest imbibition slopes (mean 0.4568) (Table 3).

3.3.2. NMR T_1-T_2 spectra

The NMR T_1-T_2 spectrum is another method for detecting fluid occurrence states (adsorbed and free) within shale pores (Zhang et al., 2020a; Liu et al., 2022b). The NMR T_1-T_2 spectra were obtained in this study to reveal the fluid occurrence states within shale pores during the SI experiments, as shown in Fig. 10. During the fast-rising stage, n-dodecane is mostly absorbed into micropores and is mostly adsorbed. Meanwhile, a small amount of free n-dodecane exists in the macropores. Following that, in the slow-rising stage, both micro- and mesopores continue to mimic n-dodecane. In micropores, n-dodecane exists primarily as an adsorbed state, whereas in mesopores, it exists as a free state. The n-dodecane is mostly free and imbibed into mesopores during the stable stage. In the fast-rising stage of LX884-1 (Fig. 10b), the adsorbed n-dodecane is predominant and primarily imbibed in micro- and mesopores. N-dodecane ingested into mesopores is mostly free, whereas n-dodecane ingested into micropores is mostly adsorbed in the slow-rising stage. Finally, some free n-dodecane was injected into the mesopores. When imbibed into

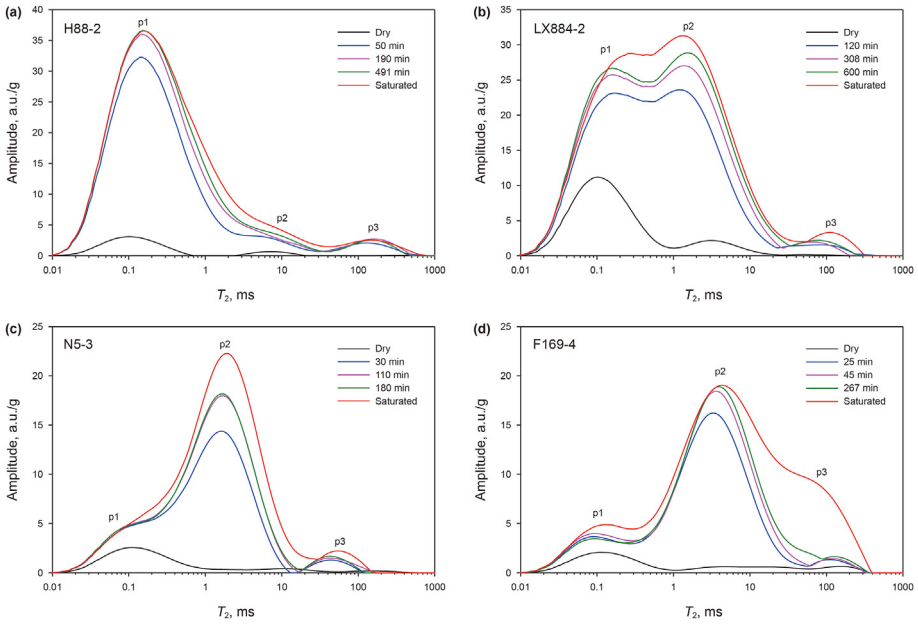

Fig. 11. NMR T_2 spectral during spontaneous imbibition and oil-saturated.

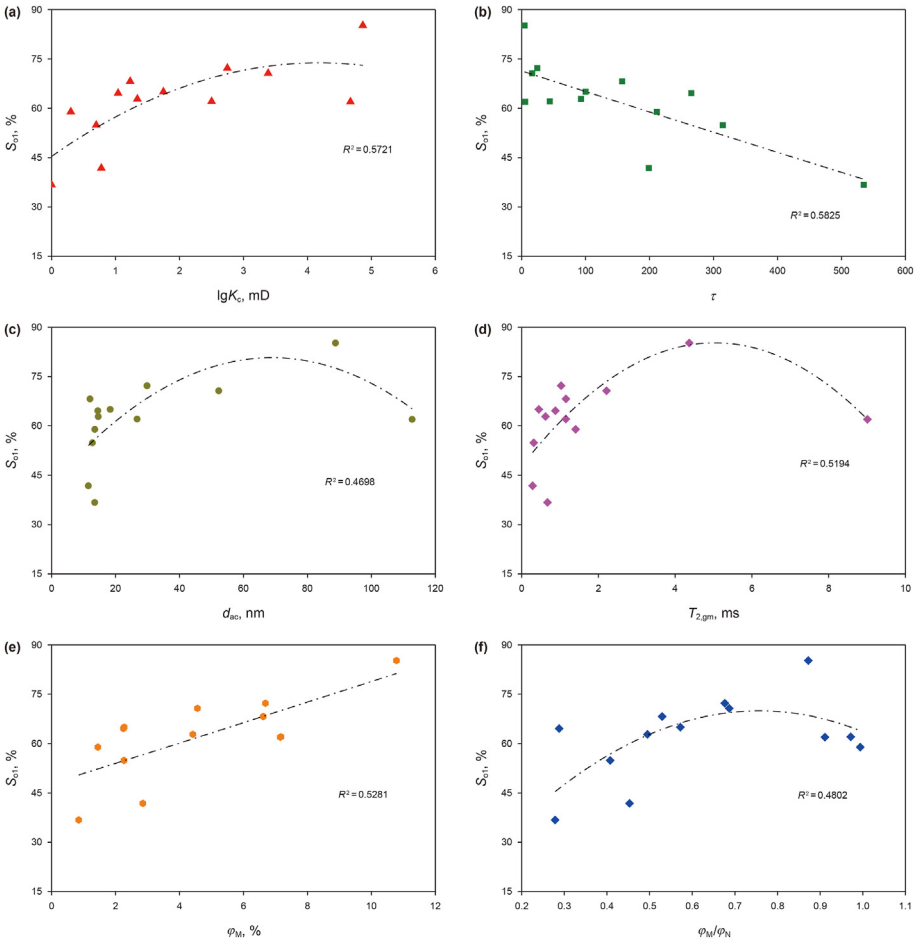

Fig. 12. Relationships between spontaneous imbibition saturation (S_{o1}) and pore structure parameters.

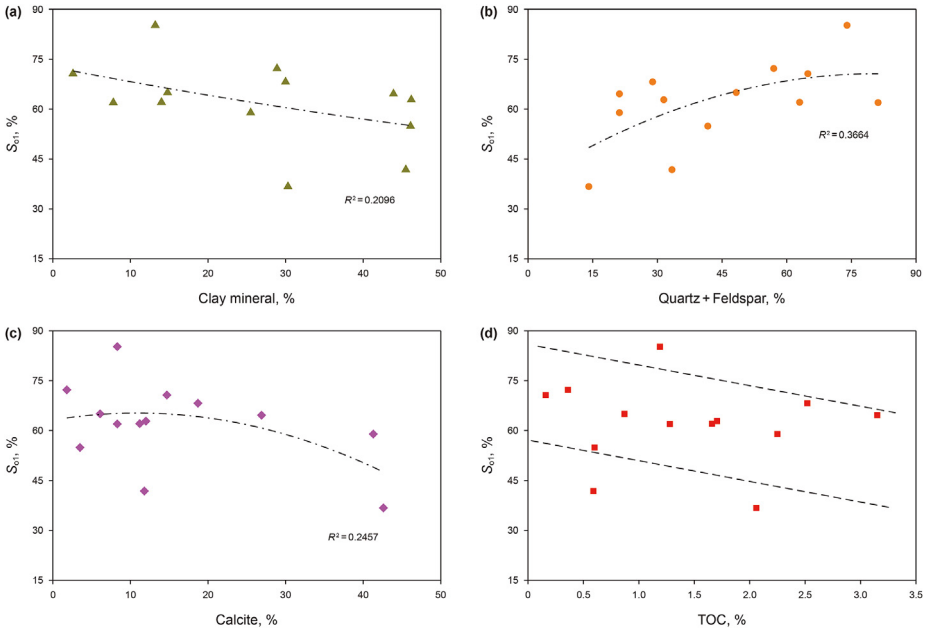

Fig. 13. Relationships between spontaneous imbibition saturation (S_{o1}) and material compositions.

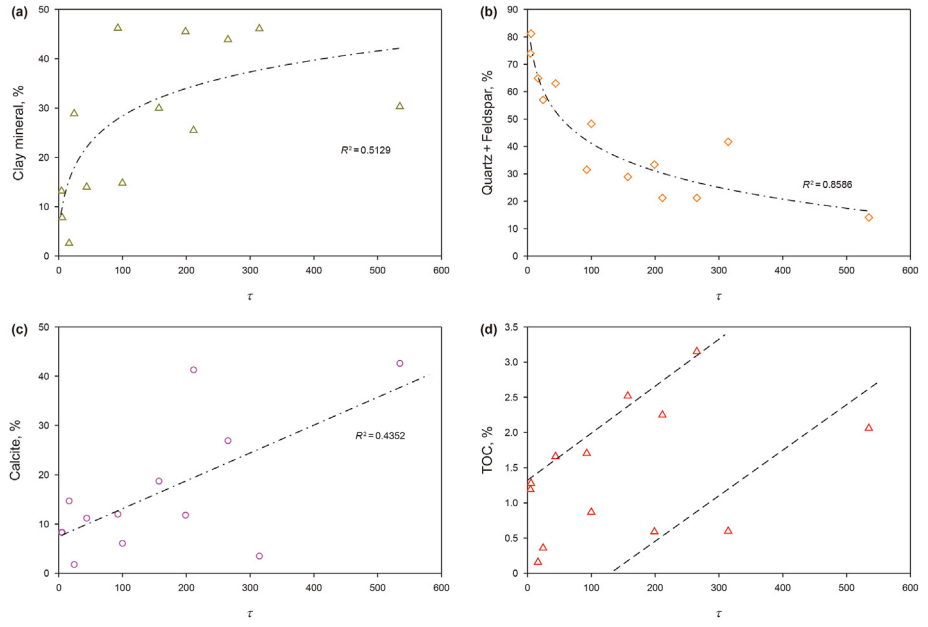

Fig. 14. Relationships between effective tortuosity (τ) and material compositions.

shale with few micropores (such as F169-4), the n-dodecane is primarily in the free state, as shown in Fig. 10d.

4. Discussion

4.1. Influence factors of spontaneous imbibition

Pore structure, organic matter, and mineral compositions are commonly used to control the SI process of shale. Fig. 11 depicts the NMR T_2 spectra of shales under dry, sequence saturation during the SI and saturated conditions. When n-dodecane imbibition is stable, p1 of the SI nearly overlaps with p1 at saturation (Fig. 11a–c), whereas the p2 of the SI is typically lower than saturated p2 (Fig. 11a–d). The amplitude of p3 at imbibition stable is much lower than that of p3 at saturation, as shown in Fig. 11d. Micropores have the highest imbibition saturation, followed by mesopores and macropores. This is because the capillary pressure decreases as one moves from micropores to macropores.

The imbibition saturation of the fast-rising stage (S_{o1}) versus pore structure parameters is shown in Fig. 12. S_{o1} and MICP permeability are positively correlated, implying that the higher the permeability, the higher the S_{o1} (Fig. 12a). The more tortuous the pore system in shale, however, the less conducive it is to fluid imbibition. As a result, a higher effective tortuosity (τ) generally results in a lower S_{o1} (Fig. 12b). The S_{o1} first increases and then decreases with the average pore-throat diameter (d_{ac}), so do the

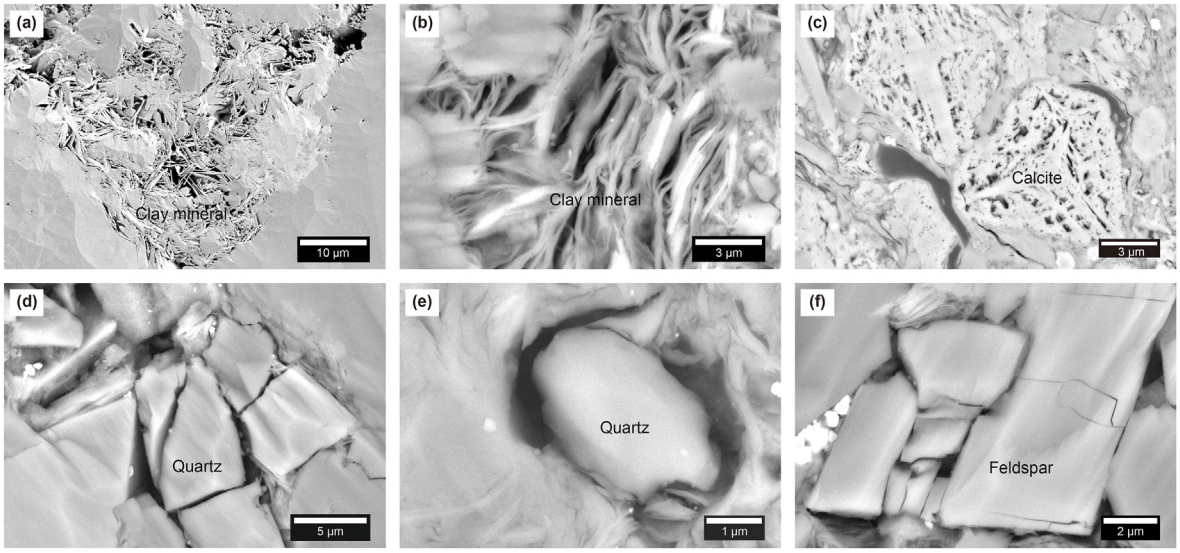

Fig. 15. SEM images of shale oil reservoirs.

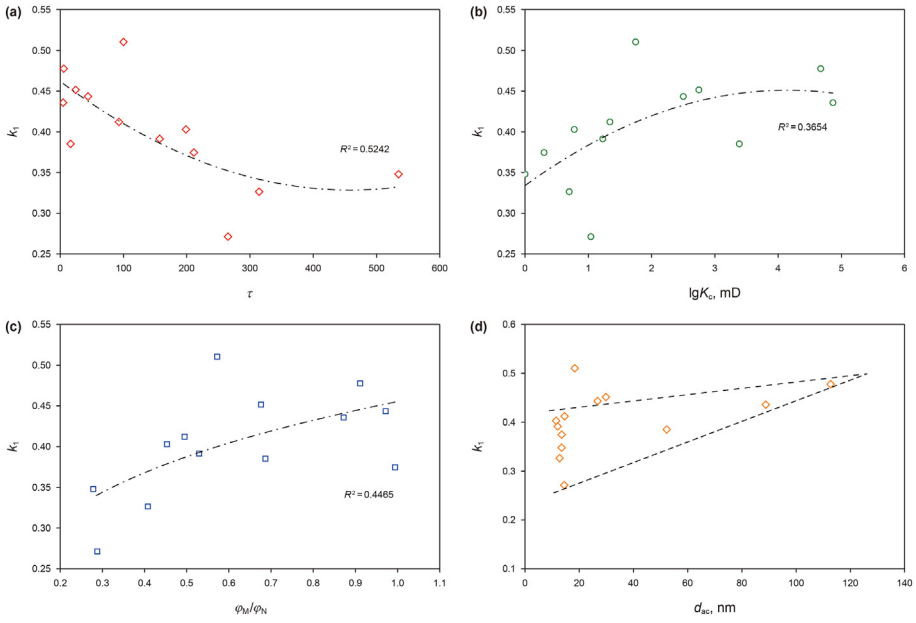

Fig. 16. Relationships between spontaneous imbibition slope (k_1) and pore structure parameters.

$T_{2,gm}$ (Fig. 12c and d). The reason for this could be that when the average d_{ac} is less than about 70 nm, as the d_{ac} increases, the better the pore connectivity, resulting in S_{o1} increasing. However, when the d_{ac} is larger than 70 nm, capillary pressure decreases rapidly as the pore (throat) size increases. As a result, a large pore (throat) size corresponds to a low capillary pressure, which leads to a lower S_{o1}. Because MICP porosity (φ_M) is the connected porosity, S_{o1} increases as the φ_M and φ_M/φ_N increase, as shown in Fig. 12e and f.

S_{o1} and clay mineral contents are negatively correlated, whereas S_{o1} and quartz and feldspar contents are positively correlated (Fig. 13a and b). Furthermore, as shown in Fig. 13c, there is a negative relationship between S_{o1} and calcite content. However, there is a slight inverse relationship between S_{o1} and TOC content (Fig. 13d). As a result, it is possible to conclude that the imbibition saturation of the shales under study is generally controlled by mineral composition rather than organic matter, as illustrated in Fig. 14. The content of clay minerals and calcite has a weakly positive correlation with effective tortuosity (Fig. 14a and c). Nonetheless, effective tortuosity and felsic mineral content (quartz and feldspar) are inversely related (Fig. 14b). Furthermore, there was a weaker positive correlation between effective tortuosity and TOC content (Fig. 14d).

It could be because intragranular pores in clay mineral aggregates and dissolution pores in calcite have complex morphology and poor connectivity. However, intergranular or grain-edge pores associated with quartz and feldspar typically have regular morphology and good connectivity, characterized by larger size, as illustrated in Fig. 15 (Zhang et al., 2018a,b; 2020b). As a result, imbibition saturation typically increases as the felsic mineral content increases while the clay mineral and calcite content decrease. Organic pores do not develop due to the lower maturity (Klaver et al., 2012; Li et al., 2015; Liu et al., 2017a,b; Wang et al., 2017).

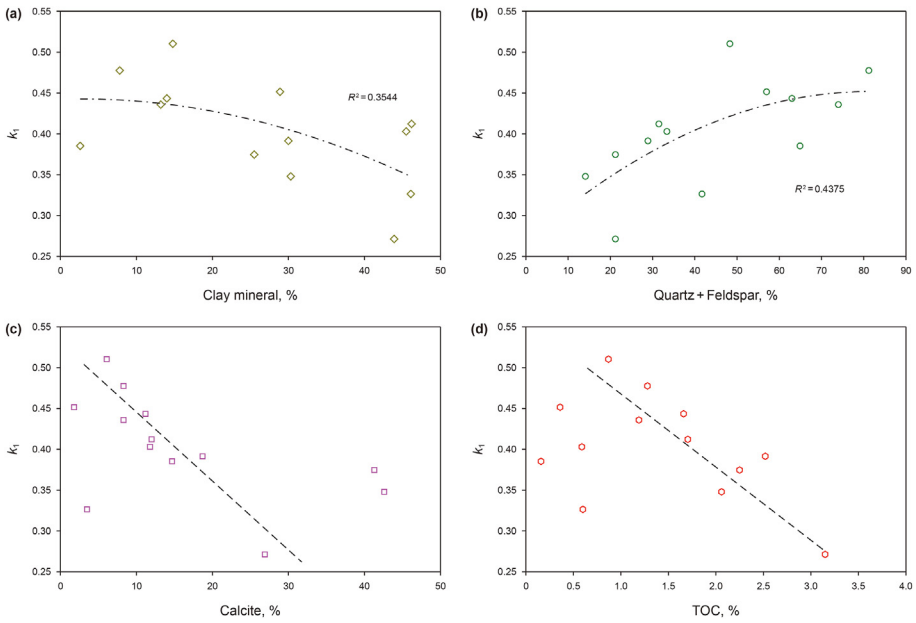

Fig. 17. Relationships between spontaneous imbibition slope (k_1) and material compositions.

Furthermore, the higher the TOC content, the more organic acid is produced during the hydrocarbon generation process, resulting in more dissolution pores in calcite (Li et al., 2018b; Kuang et al., 2022), further complicating the pore structure. As a result, a slightly negative correlation exists between S_{o1} and TOC.

4.2. Influence factors of shale pore connectivity

The fast-rising stage imbibition slope (k_1) is a critical parameter for assessing pore connectivity within the shale. Fig. 16 depicts the relationships between k_1 and pore structure parameters. The greater the effective tortuosity, the poorer the pore connectivity, as indicated by a lower k_1 value (Fig. 16a). As the MICP permeability, φ_M/φ_N, and d_{ac} increase (Fig. 16b–d), the k_1 values show an overall increasing trend, indicating progressively better pore connectivity. k_1 is positively correlated with the content of quartz and feldspar, similar to the relationship between S_{o1} and material (mineral and organic matter) components (Fig. 17b). In contrast, as shown in Fig. 17a, c-d, the k_1 values decrease as the clay mineral, calcite, and TOC contents increase.

As a result, the pore connectivity in Dongying Sag, Bohai Bay Basin shale oil reservoirs is primarily controlled by the mineral composition. Specifically, felsic minerals have large and regular pores, resulting in better connectivity; however, clay minerals and calcite have more nanoscale and complex pores, resulting in poor connectivity. Furthermore, organic matter influences pore connectivity due to diagenesis (dissolution by organic acid) during hydrocarbon generation, making the pore structure more complex and heterogeneous.

5. Conclusions

The SI-NMR experiment is an effective technology for assessing shale pore network connectivity. The counter-current SI processes of shales include three stages: fast-rising, slow-rising, and stable stages, and the fast-rising stage indicates pore connectivity. The shale oil reservoirs in the Dongying Sag, Bohai Bay Basin, have poor pore connectivity, as evidenced by lower imbibition slopes (k_1), high connected porosity ratios, and large effective tortuosity. Micropores have the highest imbibition saturation, followed by mesopores and macropores. Furthermore, the occurrence states of fluids imbibed in shale pores with different scales were revealed by the T_1-T_2 spectra. N-dodecane imbibed into micropores predominates in the absorbed state, whereas n-dodecane imbibed into mesopores and macropores predominate in the free state.

The factors that influenced pore connectivity were discovered. Shale pore connectivity is mainly controlled by inorganic minerals. Quartz and feldspar are commonly associated with large and regular pores, resulting in improved connectivity, whereas clay minerals and calcite do not because of the complex intragranular pores. Organic matter negatively impacts connectivity due to the dissolution of calcite by organic acid produced during hydrocarbon generation, which makes the pore structure more complex and heterogeneous because of intragranular dissolution pores.

Notes

The authors declare no competing financial interest.

Acknowledgments

This study was financially supported by the Natural Science Foundation of Shandong Province (ZR2020QD036, ZR2020QD037, and ZR2021QD072) and the National Natural Science Foundation of China (41972123).

References

Epstein, N., 1989. On tortuosity and the tortuosity factor in flow and diffusion through porous media. Chem. Eng. Sci. 44, 777–779. https://doi.org/10.1016/0009-2509(89)85053-5.

Gao, Z., Hu, Q., 2016. Initial water saturation and imbibition fluid affect spontaneous imbibition into Barnett shale samples. J. Nat. Gas Sci. Eng. 34, 541–551. https://doi.org/10.1016/j.jngse.2016.07.038.

Gao, Z., Yang, S., Jiang, Z., et al., 2018. Investigating the spontaneous imbibition characteristics of continental Jurassic Ziliujing Formation shale from the northeastern Sichuan Basin and correlations to pore structure and composition. Mar. Petrol. Geol. 98, 697–705. https://doi.org/10.1016/j.marpetgeo.2018.09.023.

Gao, Z., Fan, Y., Hu, Q., et al., 2019. A review of shale wettability characterization using spontaneous imbibition experiments. Mar. Petrol. Geol. 109, 330–338. https://doi.org/10.1016/j.marpetgeo.2019.06.035.

Hager, J., 1998. Steam Drying of Porous media[D]. Lund University, Sweden.

Handy, L.L., 1960. Determination of effective capillary pressures for porous media from imbibition data. AIME 219, 75–80. https://doi.org/10.1080/14786436008238345.
Huang, X., Zhao, Y., 2017. Characterization of pore structure, gas adsorption, and spontaneous imbibition in shale gas reservoirs. J. Petrol. Sci. Eng. 159, 197–204. https://doi.org/10.1016/j.petrol.2017.09.010.
Jin, Z., Zhu, R., Liang, X., et al., 2021. Several issues worthy of attention in current lacustrine shale oil exploration and development. Petrol. Explor. Dev. 48, 1276–1287. https://doi.org/10.1016/S1876-3804(21)60303-8.
Jin, Z., Liang, X., Bai, Z., 2022. Exploration breakthrough and its significance of Gulong lacustrine shale oil in the Songliao Basin, Northeastern China. Energ. Geosci. 3, 120–125. https://doi.org/10.1016/j.engeos.2022.01.005.
Katz, A.J., Thompson, A.H., 1986. Quantitative prediction of permeability in porous rock. Phys. Rev. B 34, 8179–8181. https://doi.org/10.1103/PhysRevB.34.8179.
Katz, A.J., Thompson, A.H., 1987. Prediction of rock electrical conductivity from mercury injection measurements. J. Geophys. Res. 92, 599–607. https://doi.org/10.1029/JB092iB01p00599.
Kelly, S., El-Sobky, H., Torres-Verdín, C., et al., 2016. Assessing the utility of FIB-SEM images for shale digital rock physics. Adv. Water Resour. 95, 302–316. https://doi.org/10.1016/j.advwatres.2015.06.010.
Klaver, J., Desbois, G., Urai, J., et al., 2012. BIB-SEM study of the pore space morphology in early mature Posidonia Shale from the Hils area, Germany. Int. J. Coal Geol. 103, 12–25. https://doi.org/10.1016/j.coal.2012.06.012.
Kuang, L., Hou, L., Wu, S., et al., 2022. Organic matter occurrence and pore-forming mechanisms in lacustrine shales in China. Petrol. Sci. 19, 1460–1472. https://doi.org/10.1016/j.petsci.2022.03.005.
Li, J., Shi, Y., Huang, Z., et al., 2015. Pore characteristics of continental shale and its impact on storage of shale oil in northern Songliao Basin. J. China Univ. Petrol. 29, 27–34. https://doi.org/10.3969/j.issn.1673-5005.2015.04.004.
Li, J., Lu, S., Xie, L., et al., 2017. Modeling of hydrocarbon adsorption on continental oil shale: a case study on n-alkane. Fuel 206, 603–613. https://doi.org/10.1016/j.fuel.2017.06.017.
Li, J., Lu, S., Cai, J., et al., 2018a. Adsorbed and free oil in lacustrine nanoporous shale: a theoretical model and a case study. Energy Fuel. 32, 12247–12258. https://doi.org/10.1021/acs.energyfuels.8b02953.
Li, J., Ma, Y., Huang, Z., et al., 2018b. Quantitative characterization of organic acid generation, decarboxylation, and dissolution in a shale reservoir and the corresponding applications—a case study of the Bohai Bay Basin. Fuel 214, 538–545. https://doi.org/10.1016/j.fuel.2017.11.034.
Li, X., Chen, S., Wang, Y., et al., 2022. Influence of pore structure particularity and pore water on the occurrence of deep shale gas: wufeng–longmaxi formation, luzhou block, sichuan basin. Nat. Resour. Res. 31, 1403–1423. https://doi.org/10.1007/s11053-022-10041-y.
Liu, C., Wang, Z., Guo, Z., et al., 2017a. Enrichment and distribution of shale oil in the cretaceous Qingshankou Formation, Songliao Basin, northeast China. Mar. Petrol. Geol. 86, 751–770. https://doi.org/10.1016/j.marpetgeo.2017.06.034.
Liu, Y., Lu, Z., Qi, M., et al., 2017b. Microscopic structure characteristics of shale oil reservoirs in shehejie Formation in zhanhua sag, Bohai Bay Basin. Petrol. Geol. Exper. 39, 180–182. https://doi.org/10.11781/sysydz201702180, 194.
Liu, B., Sun, J., Zhang, Y., et al., 2021. Reservoir space and enrichment model of shale oil in the first member of Cretaceous Qingshankou Formation in the Changling Sag, southern Songliao Basin, NE China. Petrol. Explor. Dev. 48, 608–624. https://doi.org/10.1016/S1876-3804(21)60049-6.
Liu, B., Jiang, X., Bai, L., et al., 2022a. Investigation of oil and water migrations in lacustrine oil shales using 20 MHz 2D NMR relaxometry techniques. Petrol. Sci. 19, 1007–1018. https://doi.org/10.1016/j.petsci.2021.10.011.
Liu, X., Guan, M., Jin, Z., et al., 2022b. Pore structure evolution of lacustrine organic-rich shale from the second member of the Kongdian formation in the Cangdong Sag, Bohai Bay Basin, China. Petrol. Sci. 19, 459–471. https://doi.org/10.1016/j.petsci.2021.12.010.
Lu, S., Xue, H., Wang, M., et al., 2016. Several key issues and research trends in evaluation of shale oil. Acta Petrol. Sin. 37, 1309–1322. https://doi.org/10.7623/syxb201610012.
Meng, M., Ge, H., Ji, W., et al., 2015a. Investigation on the variation of shale permeability with spontaneous imbibition time: sandstones and volcanic rocks as comparative study. J. Petrol. Sci. Eng. 27, 1546–1554. https://doi.org/10.1016/j.jngse.2015.10.019.
Meng, M., Ge, H., Ji, W., et al., 2015b. Monitor the process of shale spontaneous imbibition in co-current and counter-current displacing gas by using low field nuclear magnetic resonance method. J. Nat. Gas Sci. Eng. 27, 336–345. https://doi.org/10.1016/j.jngse.2015.08.069.
Ren, X., Li, A., Wang, G., et al., 2018. Study of the imbibition behavior of hydrophilic tight sandstone reservoirs based on nuclear magnetic resonance. Energy Fuel. 32, 7762–7772. https://doi.org/10.1021/acs.energyfuels.8b00768.
Tian, S., Bowen, L., Liu, B., et al., 2021. A method for automatic shale porosity quantification using an Edge-Threshold Automatic Processing (ETAP) technique. Fuel 304, 121319. https://doi.org/10.1016/j.fuel.2021.121319.
Wang, X., Shen, J., 2018. Spontaneous imbibition analysis in shale reservoirs based on pore network modeling. J. Petrol. Sci. Eng. 169, 663–672. https://doi.org/10.1016/j.petrol.2018.06.028.
Wang, Y., Pu, J., Wang, J., et al., 2016. Characterization of typical 3D pore networks of Jiulaodong formation shale using nano-transmission X-ray microscopy. Fuel 170, 84–91. https://doi.org/10.1016/j.fuel.2015.11.086.
Wang, J., Wu, W., Huang, X., 2017. Micropore structure characteristics of shale in Paleogene sha-4 member, dongying sag. J. Chin. Elect. Micr. Soc. 36, 368–375. https://doi.org/10.3969/j.issn.1000-6281.2017.04.010.
Wang, X., Peng, X., Zhang, S., et al., 2018. Characteristics of oil distributions in forced and spontaneous imbibition of tight oil reservoir. Fuel 224, 280–288. https://doi.org/10.1016/j.fuel.2018.03.104.
Wang, X., Wang, M., Li, Y., et al., 2021. Shale pore connectivity and influencing factors based on spontaneous imbibition combined with a nuclear magnetic resonance experiment. Mar. Petrol. Geol. 132, 105239. https://doi.org/10.1016/j.marpetgeo.2021.105239.
Webb, P.A., 2001. An Introduction to the Physical Characterization of Materials by Mercury Intrusion Porosimetry with Emphasis on Reduction and Presentation of Experimental Data. Micromeritics Instrument Corp, Norcross.
Wu, J., Yu, J., Wang, Z., et al., 2018. Experimental investigation on spontaneous imbibition of water in coal: implications for methane desorption and diffusion. Fuel 231, 427–437. https://doi.org/10.1016/j.fuel.2018.05.105.
Xu, L., Chang, Q., Yang, C., et al., 2019. Characteristics and oil-bearing capability of shale oil reservoir in the Permian Lucaogou Formation, Jimusaer sag. Oil Gas Geol. 40, 535–549. https://doi.org/10.11743/ogg20190309.
Xue, H., Ding, G., Dong, Z., et al., 2022. Study on the wettability and spontaneous imbibition characteristics of lacustrine shale. Geofluids 2022, 1–14. https://doi.org/10.1155/2022/4023435.
Yang, R., Hu, Q., Yi, J., et al., 2019. The effects of mineral composition, TOC content and pore structure on spontaneous imbibition in Lower Jurassic Dongyuemiao shale reservoirs. Mar. Petrol. Geol. 109, 268–278. https://doi.org/10.1016/j.marpetgeo.2019.06.003.
Zeng, F., Dong, C., Lin, C., et al., 2021. Analyzing the effects of multi-scale pore systems on reservoir properties—a case study on xihu depression, east China sea shelf basin, China. J. Pet. Sci. Eng. 203, 108609. https://doi.org/10.1016/j.petrol.2021.108609.
Zeng, F., Dong, C., Lin, C., et al., 2022. Pore structure characteristics of reservoirs of Xihu Sag in East China Sea Shelf Basin based on dual resolution X-ray computed tomography and their influence on permeability. At. Energ. 239, 122386. https://doi.org/10.1016/j.energy.2021.122386.
Zhang, P., Lu, S., Li, J., et al., 2018a. Petrophysical characterization of oil-bearing shales by low-field nuclear magnetic resonance (NMR). Mar. Petrol. Geol. 89, 775–785. https://doi.org/10.1016/j.marpetgeo.2017.11.015.
Zhang, P., Lu, S., Li, J., et al., 2018b. Permeability evaluation on oil-window shale based on hydraulic flow unit: a new approach. Adv. Geo-Energy Res. 2, 1–13. https://doi.org/10.26804/ager.2018.01.01.
Zhang, P., Lu, S., Li, J., 2019. Characterization of pore size distributions of shale oil reservoirs: a case study from Dongying sag, Bohai Bay basin, China. Mar. Petrol. Geol. 100, 297–308. https://doi.org/10.1016/j.marpetgeo.2018.11.024.
Zhang, P., Lu, S., Li, J., et al., 2020a. 1D and 2D Nuclear magnetic resonance (NMR) relaxation behaviors of protons in clay, kerogen and oil-bearing shale rocks. Mar. Petrol. Geol. 114, 104210. https://doi.org/10.1016/j.marpetgeo.2019.104210.
Zhang, P., Lu, S., Li, J., et al., 2020b. Broad ion beam-scanning electron microscopy pore microstructure and multifractal characterization of shale oil reservoir: a case sample from Dongying Sag, Bohai Bay Basin, China. Energy Explor. Exploit. 38, 613–628. https://doi.org/10.1177/0144598719893126.
Zhang, P., Lu, S., Li, J., et al., 2022. Evaluating microdistribution of adsorbed and free oil in a lacustrine shale using nuclear magnetic resonance: a theoretical and experimental study. J. Pet. Sci. Eng. 212, 110208. https://doi.org/10.1016/j.petrol.2022.110208.
Zhao, P., Wang, X., Cai, J., et al., 2019. Multifractal analysis of pore structure of Middle Bakken formation using low temperature N2 adsorption and NMR measurements. J. Petrol. Sci. Eng. 176, 312–320. https://doi.org/10.1016/j.petrol.2019.01.040.
Zheng, S., Yao, Y., Liu, D., et al., 2019. Nuclear magnetic resonance T_2 cutoffs of coals: a novel method by multifractal analysis theory. Fuel 241, 715–724. https://doi.org/10.1016/j.fuel.2018.12.044.
Zou, R., Sun, J., Li, Z., et al., 2018. Evaluating shale oil in the Dongying Depression, Bohai Bay Basin, China, using the oversaturation zone method. J. Petrol. Sci. Eng. 161, 291–301. https://doi.org/10.1016/j.petrol.2017.11.059.
Zou, C., Pan, S., Jing, Z., et al., 2020. Shale oil and gas revolution and its impact. Acta Petrol. Sin. 41, 1–12. https://doi.org/10.7623/syxb202001001.